Chemistry – A European Journal

ChemEurJ

Chemistry Europe
European Chemical Societies Publishing

RESEARCH ARTICLE

Fused-Ring Nanothread Synthesized via High-Pressure Polymerization of Naphthalene

Yunfan Fei[1] | Yajie Wang[1] | Jie Zhang[1] | Jie Liu[1] | Zilin Zhao[1] | Takanori Hattori[2] | Jun Abe[3] | Xiao Dong[4] | Ho-kwang Mao[1] | Haiyan Zheng[1] | Kuo Li[1]

[1]Center For High Pressure Science and Technology Advanced Research, Beijing, China | [2]J-PARC Center, Japan Atomic Energy Agency, Ibaraki, Japan | [3]Neutron Science and Technology Center, Comprehensive Research Organization for Science and Society, Ibaraki, Japan | [4]Key Laboratory of Weak-Light Nonlinear Photonics, School of Physics, Nankai University, Tianjin, China

Correspondence: Haiyan Zheng (zhenghy@hpstar.ac.cn) | Kuo Li (likuo@hpstar.ac.cn)

Received: 31 December 2025 | **Revised:** 15 April 2026 | **Accepted:** 21 April 2026

Keywords: [4+2] cycloaddition reaction | carbon nanothread | high-pressure | naphthalene | polycyclic aromatic hydrocarbons

ABSTRACT

Carbon nanothreads (CNThs) are one-dimensional saturated carbon nanomaterials with exceptional mechanical properties. Polycyclic aromatic hydrocarbons (PAHs) are anticipated to form thicker, multi-ring CNThs with improved mechanical performance under high-pressure. Herein, we systematically investigated the high-pressure polymerization of naphthalene, the simplest PAH, using multiple cutting-edge methods. Naphthalene molecules adopt a herringbone stacking along the *a*-*b* direction, and underwent reactions along this stacking direction above 20 GPa, affording one-dimensional unsaturated CNThs with the [4+2] cycloaddition reaction as the dominant reaction path. In contrast to the formation of many reported CNThs, the nucleation of the naphthalene-derived CNThs occurs during compression while their growth proceeds during decompression; this behavior is likely common among aromatics with a herringbone structure. The unit cell of the as-obtained CNTh crystal was determined, and a possible structure of the CNTh product was proposed. Our research reveals the polymerization characteristics of naphthalene under high-pressure, highlighting that the slip-angle and herringbone-angle play an important role in governing the polymerization pathway.

1 | Introduction

Carbon nanothreads (CNThs), a class of one-dimensional (1D) carbon materials, exhibit exceptional mechanical performance and thermal conductivity [1–8]. By slow compression-decompression of a benzene crystal under uniaxial stress, CNTh with pseudohexagonal packing was first synthesized [9, 10]. However, the internal structure of this nanothread was disordered. Further studies have revealed [11–13] that benzene-derived nanothreads contain multiple intrathread structures, which are formed via several plausible reaction pathways such as the [4+2] cycloaddition reaction and 1-1' bonding. In subsequent research, more ordered nanothreads have been achieved by introducing substituents or heteroatoms into benzene rings as precursor molecules, including phenol [14], trifluorobenzene [15, 16], pyridine [17], pyridazine [18], thiophene [19], and furandicarboxylic acid [20], and so forth.

It has been reported that CNThs derived from polycyclic aromatic hydrocarbons (PAHs) exhibit larger diameters than benzene-derived analogs, thereby endowing them with superior mechanical properties [21]. However, the synthesis of PAH-based nanothreads is a process significantly more complex than that of monocyclic aromatics. For monocyclic aromatics, molecules capable of forming ordered CNThs are often stacked in parallel columns. In contrast, PAHs possess much more complex molecular structures

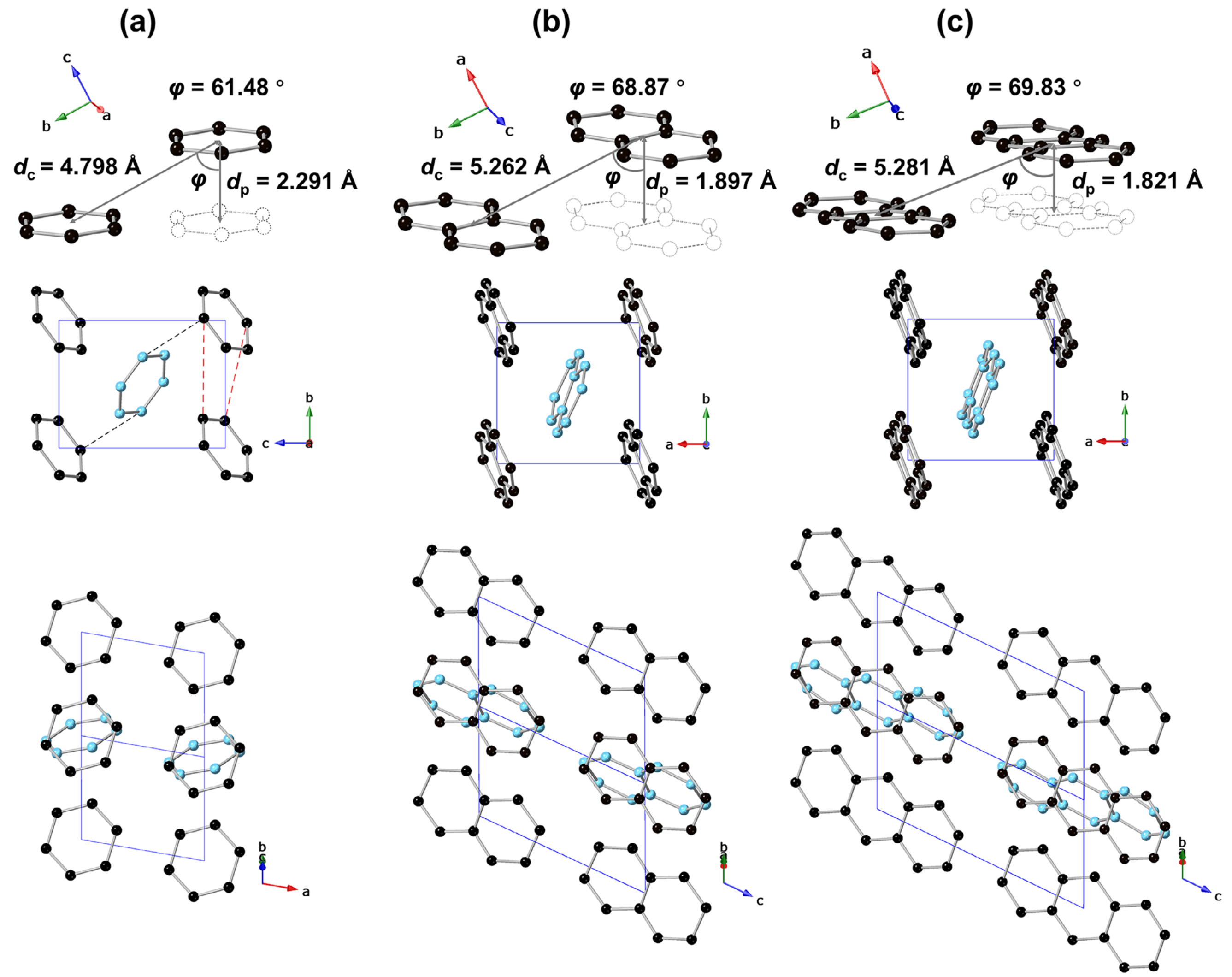

FIGURE 1 | The arrangement of molecules along the *b* direction (top) and stacking (middle and bottom) of (a) benzene phase II, (b) naphthalene, and (c) anthracene in a crystal at 20 GPa. The hollow and dashed molecule represents the projection of the molecule in the above layer. The red and black dashed lines show the polymerization routes of benzene along the *b* and *b-c* directions, respectively. Hydrogen atoms were omitted. The corresponding neutron diffraction data are shown in Figures S1, 5, S12, and S2.

and intermolecular interactions, which regulate molecular stacking and polymerization reaction pathways. For instance, azulene adopts an antiparallel columnar stacking arrangement due to the dipole-dipole interaction, and the obtained CNThs exhibit ordered interthread packing while their intrathread structure remains disordered [22]. By introducing hydrogen bonding or quadrupole interactions, naphthalene/octafluoronaphthalene and anthracene/octafluoronaphthalene [23, 24] are stacked in column and polymerize into CNThs with improved ordering. On the other hand, biphenylene molecules with herringbone arrangement polymerize to form nanoribbons [25].

The spatial relationships between adjacent molecules in aromatic hydrocarbon crystals are described by the distance between ring centroids (d_c), the distance between ring planes (d_p), and the slip angle (φ), as shown in the top of Figure 1a–c. When φ is small, the molecules are arranged approximately in a column and the reaction proceeds along the axis of the column. When φ is larger, the molecules often form herringbone arrangement, and the reaction pathway will change, like para-polymerization of biphenylene [25]. Taking benzene as a reference, benzene has a herringbone structure in phase II, and φ is 61.48° at 20 GPa [26], which is likely to polymerize via [4+2] cycloaddition along π-π stacking in the *b* direction or 1,4-polymerization along herringbone stacking in the *b-c* direction above 20 GPa (the middle of Figure 1a) [27]. Linear PAHs have the similar herringbone structure (Figure 1) [28] and φ and d_c are larger than that of benzene (68.87° for naphthalene and 69.83° for anthracene at 20 GPa, respectively). Obviously, a larger φ angle and d_c are unfavorable for reaction along the *b* direction (the original columnar π-π stacking direction). The effect of PAH stacking on the reaction pathways and product structures merits systematic investigation, which plays the most important role in the synthesis of CNThs.

As the simplest PAH, naphthalene undergoes a slight phase transition at about 3 GPa as indicated by spectroscopic data [29, 30]. In situ X-ray diffraction results demonstrate that this phase transition does not involve structural reconstruction. Naphthalene retains its monoclinic structure ($P2_1/a$) [31–33], oligomerizes above 15 GPa [33], and amorphizes irreversibly above 30 GPa [29].

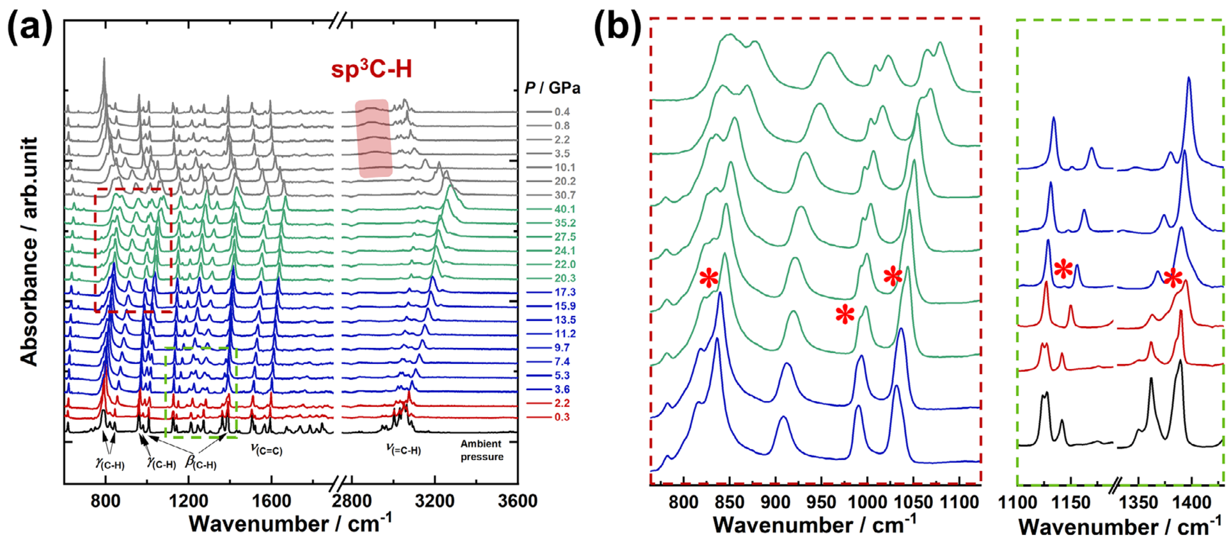

FIGURE 2 | (a) In situ IR spectra of naphthalene under compression and decompression process. The spectral range of 1900–2750 cm^{-1} was omitted due to the strong absorption of the diamond. (b) The enlarged views inside the dashed box. The asterisks represent the appearance of new peaks. ν, γ, and β represent the stretching, out-of-plane bending, and in-plane bending vibration, respectively.

In a recent study, ordered nanothread products were synthesized by slowly applying uniaxial stress to naphthalene in the diamond anvil cell (DAC). Several fully saturated nanothread models were proposed whose backbones differ distinctly from those of naphthalene/octafluoronaphthalene-derived nanothreads [34]. In this work, we successfully synthesized the bulk ordered naphthalene-derived carbon nanothreads and systematically investigated their long-range structure and reaction mechanism using a series of cutting-edge characterization techniques. We demonstrated that naphthalene formed 1D unsaturated CNThs above 20 GPa with the [4+2] cycloaddition reaction as the dominant pathway. Notably, naphthalene begins to polymerize upon reaching the threshold reaction pressure, and continues to complete the reaction during decompression (propagation/growth and termination). This reaction mechanism is likely prevalent in the polymerization of other PAH crystals with a herringbone packing structure.

2 | Results and Discussion

2.1 | High-Pressure Reactivity of Naphthalene

In situ infrared (IR) spectroscopy experiments were performed to investigate the high-pressure polymerization process of naphthalene, and the assignments of the selected IR modes are shown in Figure S3 based on the theoretical calculation. As shown in Figure 2, two new peaks at 1143 and 1387 cm^{-1} ascribed to C—H in-plane bending vibration, appeared at 2.2–3.6 GPa, suggesting a phase transition around 3 GPa, consistent with previous literature [29]. The further changes occur above 20 GPa, where new characteristic peaks in the region of C—H out-of-plane bending vibration emerged at 831, 992, and 1038 cm^{-1}, indicating a phase transition or chemical reaction.

To further determine the polymerization reaction, the samples recovered from different pressure conditions were analyzed (Figure S4). The results show that, without prolonged pressure maintenance, the significant sp^3 C—H stretching vibration peak, as the characteristic peak of the polymerization reaction, was observed only in the sample recovered from 40 GPa. In contrast, after prolonged pressure maintenance, this signal was detected in the sample recovered from 23 GPa. This observation unambiguously confirmed prolonged pressure maintenance facilitates the polymerization. Furthermore, regardless of the maximum pressure reached or its duration, polymerization signals appear exclusively during decompression (Figure S4 and the red transparent region in Figure 2a), which is different from the polymerization of naphthalene-octafluoronaphthane co-crystal [24]. Moreover, single-crystal naphthalene didn't initiate polymerization even when subjected to the pressure of up to 30 GPa and heated to 300°C (Figure S5). These results indicate that the polymerization occurs mainly during decompression and is directly affected by grain boundaries or crystal defects. Based on these observations, we proposed that after reaching the pressure threshold, polymerization is initiated to form "seeds" at grain boundaries or crystal defect sites. Prolonged pressure maintenance at relatively lower pressure or the application of higher pressure promotes the generation of more "seeds", which is essential for the occurrence of extensive polymerization during decompression. Subsequently, during decompression, the increase in molecular free space allows more frozen molecules to be reoriented to orientations favorable to reaction progression. These molecules then undergo polymerization of sp^2-hybridized carbon to form sp^3-hybridized carbon, facilitating further growth of the polymerization product. Similar features are also observed among aromatics with herringbone structure, such as benzene [9, 35], 1,4-difluorobenzene [26], and biphenylene [25], and so forth.

2.2 | Synthesis and Crystallographic Analysis of Polymerization Product

To characterize the structure of the polymerization product, we synthesized samples using a Paris–Edinburgh (PE) press at

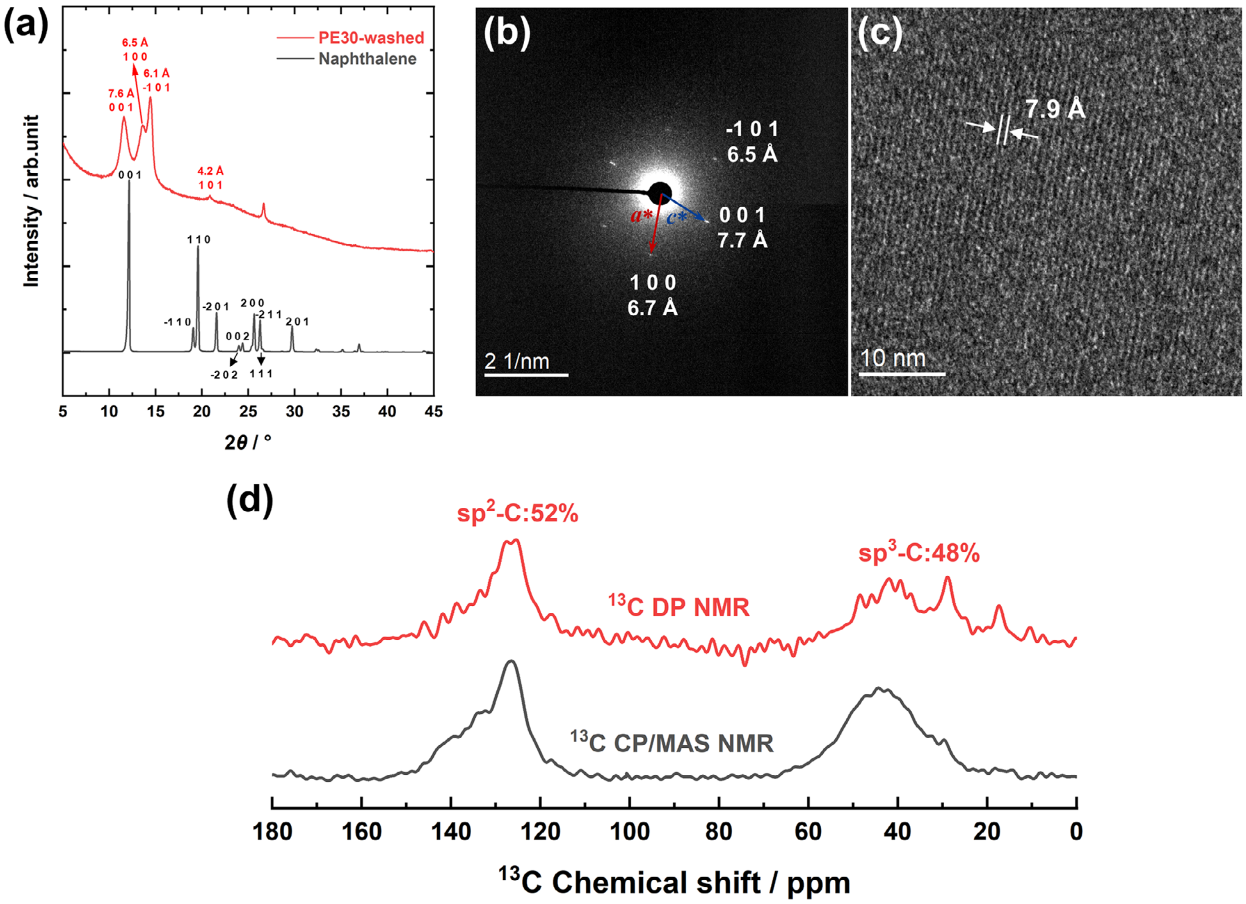

FIGURE 3 | (a) XRD of PE30-washed and naphthalene. (b) The selected electron diffraction results and (c) high-resolution TEM results of PE30-washed. (d) ^{13}C CPMAS and DP solid-state NMR spectra of PE30-washed.

30 GPa and removed the unreacted naphthalene via washing with *n*-hexane (referred to as PE30-washed). IR spectra of naphthalene and the PE30 sample before and after washing confirm the complete removal of naphthalene (Figure S6). IR spectra and X-ray diffraction (XRD) patterns of the 30 GPa products synthesized by DAC and PE press (Figure S7) demonstrate that the products synthesized by these methods are identical. The XRD analysis (Figure 3a) of the PE30-washed shows clear diffraction peaks at the *d*-spacing of 7.6, 6.5, 6.1, and 4.2 Å, respectively, confirming the ordering in the product. In consistency with the XRD result, the obvious two-dimensional ordering with pseudohexagonal symmetry (Figure 3b) is observed in the selected area electron diffraction (SAED). This demonstrates the formation of nanothreads with pseudohexagonal arrangement, similar to those CNThs derived from benzene [10], trifluorobenzene [15, 16], and pyridine [17]. The peaks are indexed as 001 (d_{001} = 7.7 Å), 100 (d_{100} = 6.7 Å), and −101 (d_{-101} = 6.5 Å), respectively, and the two-dimensional lattice is determined as a = 6.9696(8) Å, c = 8.1615(9) Å, and β = 110.740(6)° by Le Bail fitting of XRD data. The high-resolution TEM images of the product also display distinct parallel lattice fringes with a *d*-spacing of about 7.9 Å, corresponding to the (001) planes and confirming 1D thread structure (Figure 3c). These features are consistent with the high-pressure polymerization products of benzene [9, 10] and trifluorobenzene [15, 16]. All the results indicate that the product of naphthalene is a 1D CNTh with pseudohexagonal packing.

2.3 | The Intrathread Structure and Reaction Mechanism of Polymerization Product

To investigate the intrathread structure and reaction mechanism of the product, we performed ^{13}C cross-polarization magic angle spinning (CP/MAS) and quantitative full relaxed direct-polarization (DP) solid-state nuclear magnetic resonance (ssNMR) measurements on PE30-washed. The ^{13}C CP spectrum (Figure 3d) exhibits signals in both the sp^2 carbon region (110–150 ppm) and sp^3 carbon region (20–70 ppm). The DP result shows the product contains 52% sp^2 carbon and 48% sp^3 carbon, meaning on average ∼5 sp^2 carbons of each naphthalene molecule are converted to sp^3 carbons during the polymerization process.

Subsequently, we investigated the pressure-induced bonding pathway of naphthalene by using Gas Chromatography-Mass Spectrometry (GC-MS). Given the insufficient quantity of oligomers extracted from PE30 for analysis, we synthesized sample PE20 using PE press at 20 GPa. IR spectra show that the product recovered from 20 GPa is the same as those recovered from 30 GPa (Figure S8). PE20 was dissolved in dichloromethane for GC-MS measurements. Components with an abundance exceeding 0.1% were compared with a standard sample or recognized by searching in the National Institute of Standards and Technology (NIST) /Wiley standard library. As

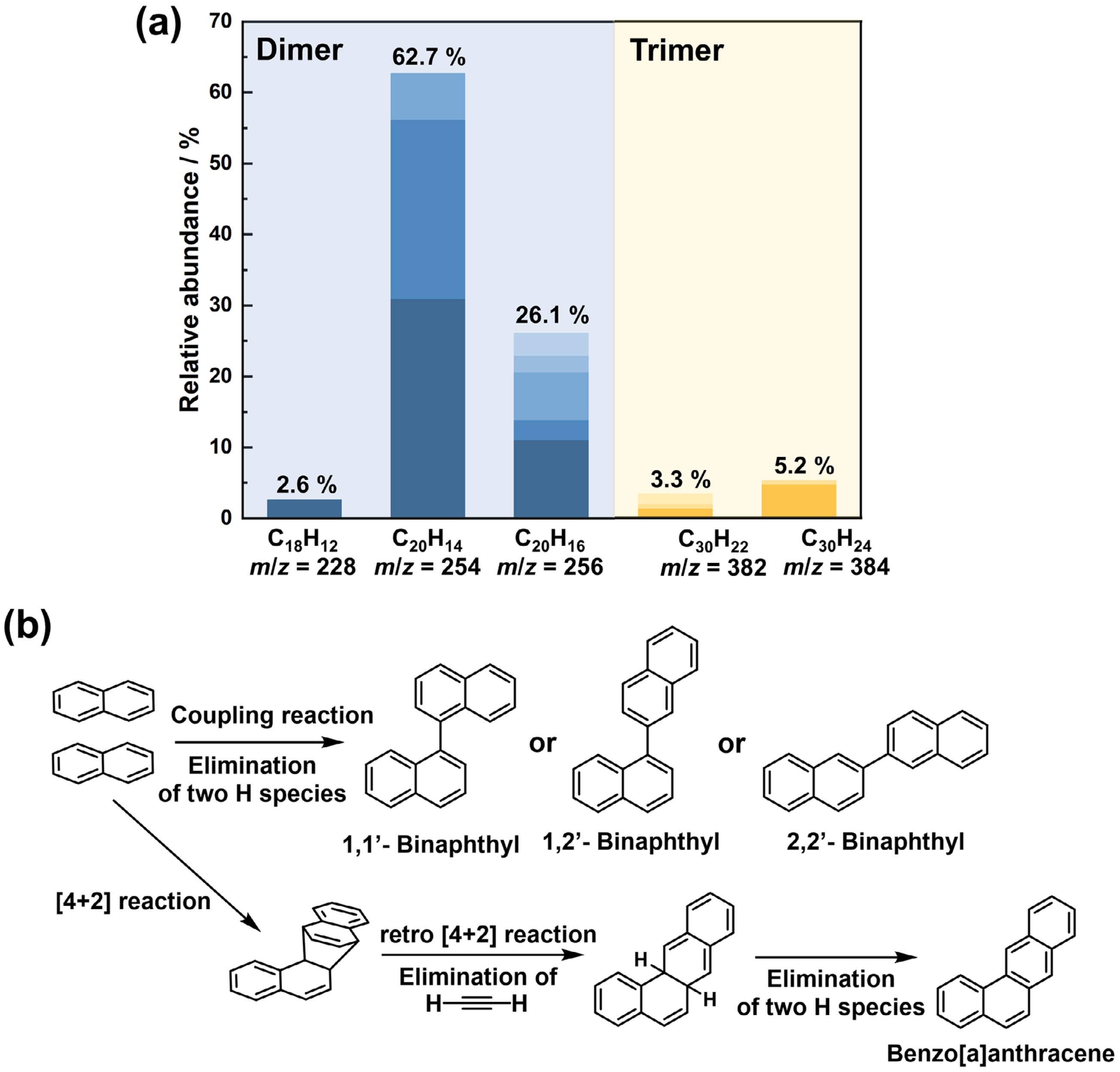

FIGURE 4 | (a) Relative content of primary identifiable oligomers with abundance above 0.1% in supernatant of PE20 detected by GC-MS. (b) Proposed reaction paths of naphthalene dimers under high-pressure.

shown in Figure 4a, nine naphthalene dimers (m/z = 228, 254, and 256) and five trimers (m/z = 382 and 384) were detected alongside naphthalene. The component of m/z = 228 and three isomers of m/z = 254 are clearly identified as benzo[a]anthracene, 1,1'-binaphthyl, 1,2'-binaphthyl, and 2,2'-binaphthyl, respectively (Figure S9a,b). The mass spectra of five isomers with m/z = 256 are similar to that of 3,4-dihydro-1,1'-binaphthalene ($C_{20}H_{16}$) (Figure S9c), but their exact structures cannot be determined due to the lack of corresponding standard samples. Notably, 1,1'-binaphthyl was the most abundant binaphthyl isomer, not 1,2'-binaphthyl as reported in previous literature [33]. As shown in Figure 4b, benzo[a]anthracene is formed via a [4+2] pericyclic reaction between two naphthalene molecules, followed by a retro-[4+2] reaction as well as the elimination of two bridgehead hydrogen atoms; binaphthyl isomers are generated through the coupling reaction. These results confirm that [4+2] pericyclic reactions and coupling reactions are the two primary pathways in naphthalene polymerization. Similar dimerization mechanisms have also been reported for the pressure-induced dimerization of benzene at room temperature above 13 GPa [16, 36].

For the trimers, three isomers at m/z = 382 and two isomers at m/z = 384 were identified (Figure S9d,e). Most of them display a weak molecular ion (M^+) peak and intense characteristic radical cation fragments at m/z = 228 ($C_{18}H_{12}$) or m/z = 128 ($C_{10}H_8$), as shown in the mass spectra at retention times of 126.10, 118.22, 117.18, and 117.04 min (Figure S9d). These features are consistent with [4+2] cycloaddition products, such as the fluorobenzene trimer formed via [4+2] cycloaddition [16], which exhibit weak M^+ peaks accompanied by prominent characteristic fragment peaks generated via retro Diels-Alder (rDA) fragmentation. This strongly suggests that the [4+2] reaction is involved in the formation of all these trimers (the proposed fragmentation pathways are shown in Figure S10). The distinct retention times and mass spectra arise from structural differences among the trimers, which originate from varying reaction sites on the dienophile (Figure S9d). Notably, $C_{30}H_{22}$ ($m/z = 382$) at a retention time of 123.32 min is the trimmer with one H—H molecule eliminated. It's likely formed via a sequential [4+2] cycloaddition and 1,1'-coupling reaction, as supported by the release of $C_{20}H_{14}$ ($m/z = 254$) and $C_{18}H_{12}$ ($m/z = 228$) fragments. This implies that the coupling reaction may also contribute to the formation of this specific trimer, analogous to the previously reported fluorobenzene trimer [16]. Nevertheless, [4+2] cycloaddition accounts for the majority of the trimers, and we therefore conclude that it represents the predominant pathway for trimer formation.

Based on the above analysis, we infer that both the [4+2] cycloaddition and coupling reactions are involved in the formation of dimers. Among the dimers, the abundance of dimers generated via the [4+2] cycloaddition reaction accounts for only 2.6% (Figure 4a), significantly lower than that of dimers formed through the coupling reaction. For trimers, the [4+2] cycloaddition participates in the formation of all trimers, whereas the coupling reaction only contributes to a specific trimer at a retention time of 123.32 min. This confirms that [4+2] cycloaddition is the predominant pathway for trimer formation. Using the direct-entry probe mass spectrometry (DEP-MS), higher-degree oligomers, including the tetramers, can also be detected. The ratio of products formed via pure [4+2] reaction ($C_{10n}H_{8n}$, n = 2, 3, 4) relative to those formed via [4+2] reaction accompanied by 1,1'-coupling reaction ($C_{10n}H_{8n-2}$, n = 2, 3, 4) increased with increasing polymerization degree (Figure S11). All these results confirmed that as the degree of polymerization increases, the coupling reaction is gradually suppressed, while the [4+2] reaction becomes the prevailing pathway in the synthesis of CNTh.

As revealed by the ssNMR data, an average of approximately five carbon atoms per naphthalene unit participate in the reaction. We therefore conclude that the four sp^2-hybridized carbon atoms in each naphthalene molecule undergo two [4+2] cycloaddition reactions and transform into sp^3-hybridized carbons. Additional [4+2] cycloaddition reactions also take place, resulting in the polymerization of a total of about five sp^2-hybridized carbons. Accordingly, the internal structure of naphthalene-derived CNTh consists of a mixture of structures with saturation degrees of 6 and 4 (where the saturation degree is defined as the number of saturated carbon atoms per $C_{10}H_8$ unit in the nanothread). This is distinct from the fully saturated naphthalene-derived nanothread reported in previous studies [34].

2.4 | High-Pressure Structure Evolution and Product Models

We subsequently carried out in situ neutron diffraction measurements on naphthalene-d_8 up to 20 GPa to investigate the structure evolution of naphthalene under compression. At ambient temperature and pressure, naphthalene crystallizes in a monoclinic system with the space group $P2_1/a$, where the unit cell parameters are $a = 8.2577(5)$ Å, $b = 5.9798(4)$ Å, $c = 8.6638(6)$ Å, and $\beta = 122.727(4)°$. Each unit cell contains two naphthalene molecules arranged in a herringbone stacking. As shown in Figure 5a, upon compression to 20.0 GPa, all the diffraction peaks are weakened and shifted toward low d-spacing, which arises from the reduction in intermolecular distances under high-pressure. Rietveld refinements were then performed on all collected diffraction data, confirming that naphthalene-d_8 maintains its monoclinic phase throughout the entire pressure range of 0–20 GPa. Figure 5b illustrates the evolution of the lattice parameters up to 20 GPa, revealing a discontinuity in lattice parameters at 3.2 GPa. A corresponding discontinuity is also observed in the P-V data at 3.2 GPa. Further detailed analysis of the high-pressure crystal structure of naphthalene shows that the herringbone angle (defined as the angle between the molecular planes along the herringbone-stacking direction, as shown in Figure S13b) [32] decreases rapidly with increasing pressure below 3 GPa, but varies only slightly above 3 GPa (remaining at 44±1°), as shown in Figure S12a. This behavior likely corresponds to the observed weak phase transition. For the pressure range of 3.2–20.0 GPa, we fitted the P-V data using the third-order Birch–Murnaghan equation of state (Figure 5c):

$$P(V) = \frac{3}{2}B_0\left[\left(\frac{V_0}{V}\right)^{7/3} - \left(\frac{V_0}{V}\right)^{5/3}\right]\left\{1 + \frac{3}{4}(B_1 - 4)\left[\left(\frac{V_0}{V}\right)^{2/3} - 1\right]\right\} \tag{1}$$

where, V_0 is the unit cell volume at ambient pressure, B_0 and B_1 are the isothermal bulk modulus and its first pressure derivative. The result shows $V_0 = 316 \pm 4$ Å^3, $B_0 = 26 \pm 4$ GPa and $B_1 = 4.0 \pm 0.4$.

The crystal structure of naphthalene-d_8 at 20 GPa was determined via Rietveld refinement (Figure S12b), followed by density functional theory (DFT) optimization with the lattice parameters fixed at the experimental values (space group $P2_1/a$, $a = 6.69$ Å, $b = 5.26$ Å, $c = 7.85$ Å, $\beta = 127.23°$). As shown in Figure 5d, naphthalene molecules still adopt a herringbone stacking at 20 GPa. The shortest intermolecular carbon-carbon (C—C) distance is 2.751 Å (marked in red), followed by 2.899 Å (yellow), 2.900 Å (green), and 2.944 Å (blue), which are all close to the typical threshold distance of the aromatic molecules [37]. Notably, most of these short intermolecular distances occur between the molecules aligned along the a-b direction. Thus, we hypothesize that naphthalene may undergo chemical reactions preferentially along the a-b direction, which is consistent with the predicted reaction direction based on molecular stacking.

Based on the above experimental results, the possible product models were constructed via two consecutive [4+2] cycloaddition reactions along the a-b direction with its initial structure derived from the crystal structure of naphthalene at 20 GPa. Models P1 and P2 were built by performing two [4+2] cycloaddition reactions on a single benzene moiety within the naphthalene molecules, whereas models P3 and P4 were constructed by carrying out one [4+2] cycloaddition reaction on each of the two benzene units (Figure 6a). Subsequent structural optimizations were performed with the lattice parameters relaxed under ambient pressure. The interplanar spacings of the resulting nanothread products were compared with the calculated results of the models. As shown in Figure 6b, the simulated d-spacings of the (001), (100) and (−101) crystal planes of model P1 agree best with the experimental data, followed by P2, while P3 and P4 show significantly poorer agreement. This indicates that naphthalene preferentially polymerizes on a single benzene ring moiety, and

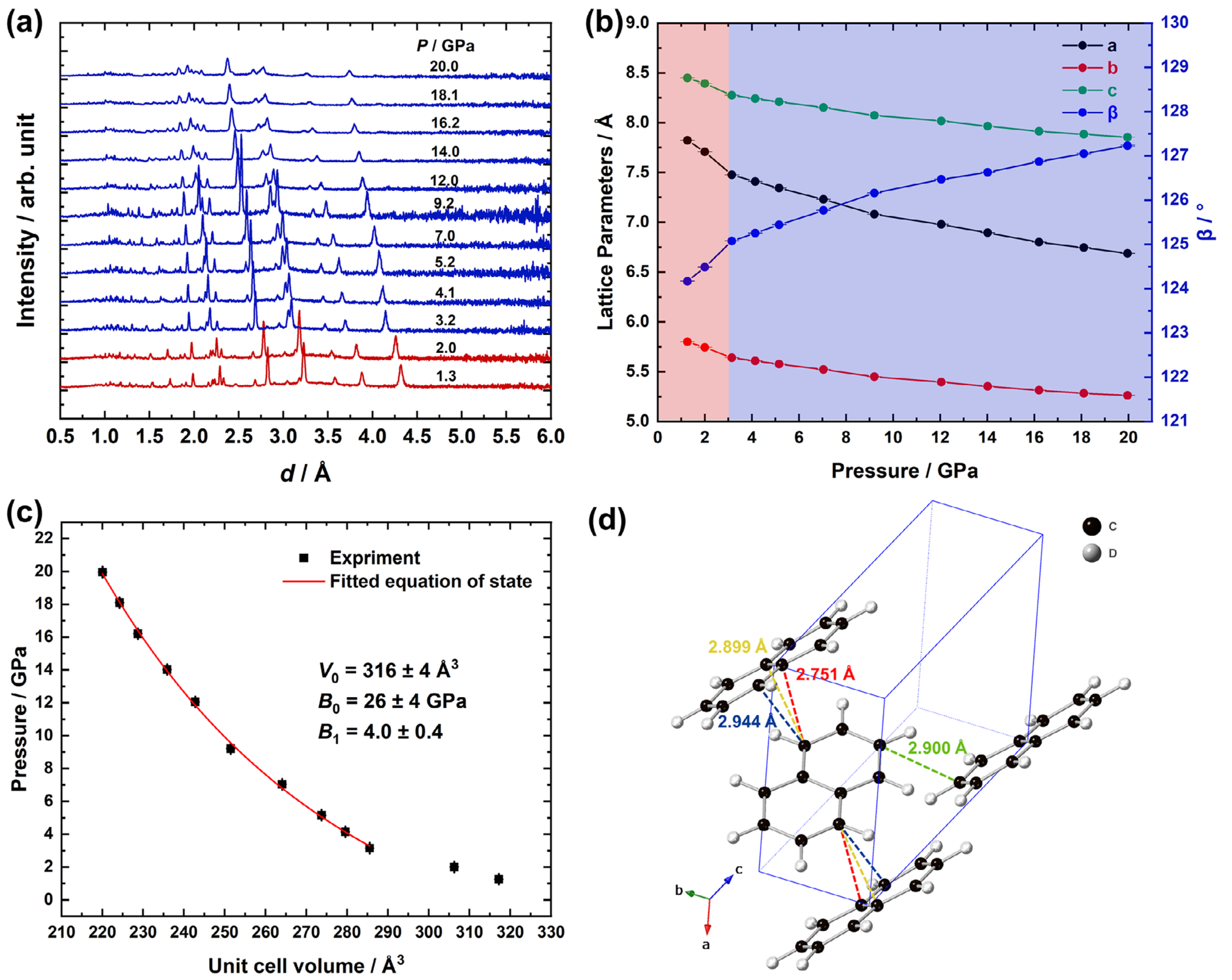

FIGURE 5 | (a) In situ neutron diffraction patterns and (b) the evolution of lattice parameters of naphthalene-d_8 under high-pressure. (c) *P-V* relations for naphthalene-d_8 fitted with the third-order Birch-Murnaghan equation of state with $V_0 = 316 \pm 4$ Å^3, $B_0 = 26 \pm 4$ GPa and $B_1 = 4.0 \pm 0.4$. (d) The crystal structure of naphthalene-d_8 at 20 GPa.

P1 represents the most plausible structure for the polymerized product. Its packing and the atomic coordinates after unit cell conversion are shown in Figure 6c and Table S2. Furthermore, the simulated IR spectrum of model P1 matches well with the experimental spectrum (Figure 6d). The experimental IR spectrum exhibits characteristic peaks at about 3030^{-1}, 1480^{-1}, and 770 cm^{-1}, which are assigned to the sp^2 C—H stretching vibration, the C═C stretching vibration, and the sp^2 C—H out-of-plane bending vibration, respectively. This once again confirms that the naphthalene-derived carbon nanothread is unsaturated.

For linear PAHs with a herringbone arrangement, it's worthy to analyze the slip angle φ and the herringbone angle θ (Figure S13). A larger slip angle φ and the distance between ring centroids d_c tend to suppress the reactions along the π-π stacking direction, whereas a smaller herringbone angle θ promotes the reaction along the herringbone-stacking direction. For example, naphthalene exhibits a larger slip angle than benzene, while the herringbone angle at 20 GPa follows the order: benzene (57.05°) > naphthalene (42.26°) > anthracene (40.34°). This structural feature likely enhances the reaction selectivity of naphthalene toward polymerization along the *a*-*b* (herringbone stacking) direction. Similarly, other linear PAHs with larger slip angle φ and the distance between ring centroids d_c and a smaller herringbone angle θ, such as anthracene, should also undergo reaction along the herringbone-stacking in the *a-b* direction. It should be clarified that now we can only conclude that the reaction is initiated along the *a-b* direction. The propagation of the CNTh is likely to happen during decompression, and its growth direction remains to be determined.

3 | Conclusion

In summary, we have investigated the high-pressure polymerization of naphthalene and found that it undergoes reaction along the herringbone stacking direction (the *a-b* direction) above 20 GPa. The [4+2] cycloaddition constitutes the dominant reaction pathway, yielding an unsaturated carbon nanothread (CNTh) product with a well-defined unit cell. Upon

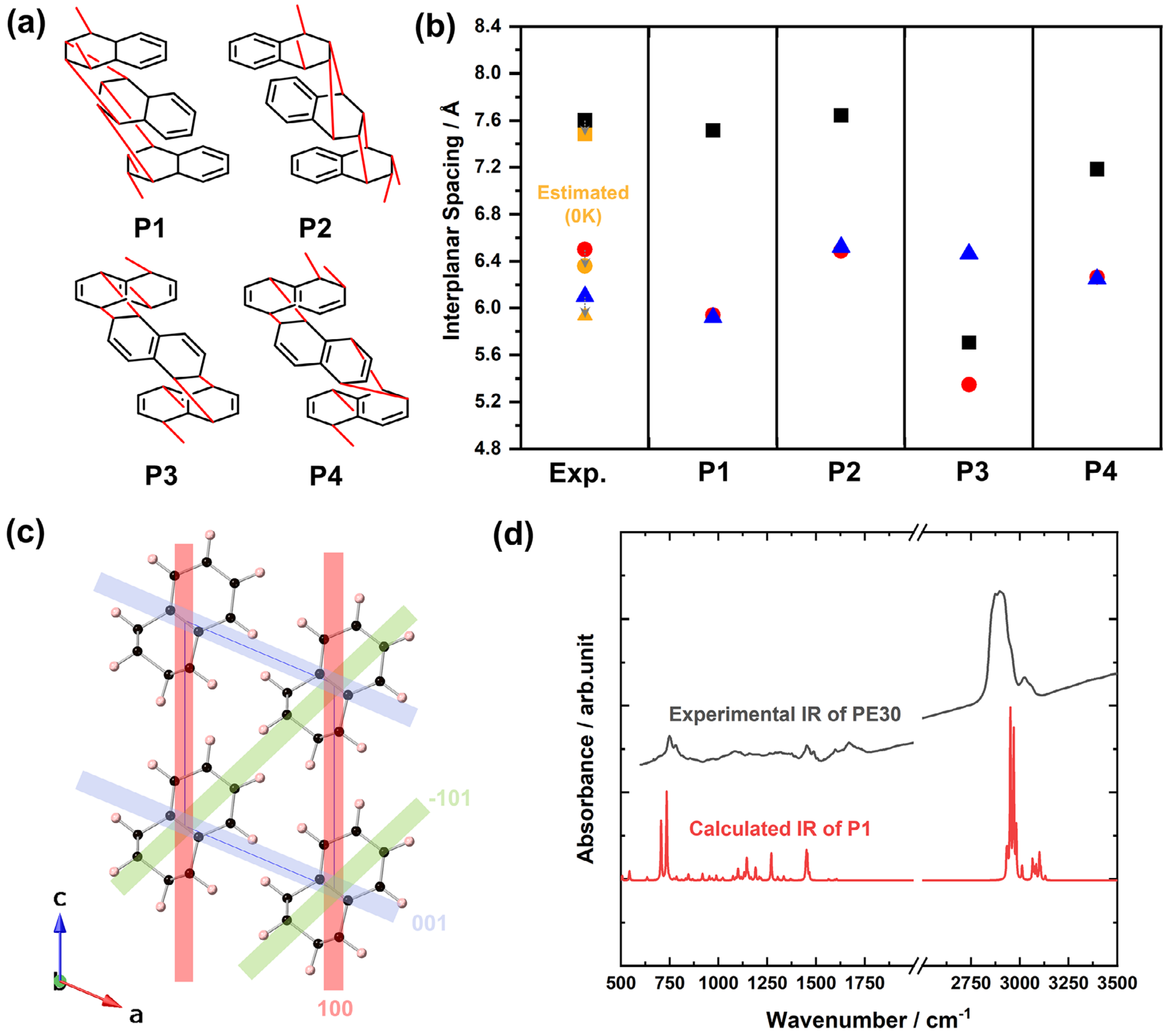

FIGURE 6 | (a) The bonding diagrams along the *a*-*b* direction when constructing the models. (b) Experimental and simulated interplanar spacings of carbon nanothread, and the experimental data have been adjusted for thermal expansion. The square, dot, and triangle represent d_{001}, d_{100}, and d_{-101}, respectively. (c) The two-dimensional packing of P1 projected along the *b* direction. (d) IR spectra of PE30-washed (experiment) and P1 model (calculation).

reaching the reaction threshold pressure, naphthalene initiates polymerization to form “reaction seeds”, and the resulting CNTh further propagates and grows during decompression. This work provides deeper insights into the physicochemical behavior of polycyclic aromatic hydrocarbons under high-pressure conditions.

4 | Experimental Section

4.1 | Sample Preparation and High-Pressure Generation

Naphthalene was purchased from Innochem and used without further purification. For all the high-pressure in situ experiments, the symmetric diamond anvil cell (DAC) with an anvil culet size of 300 µm in diameter was used. Type-IIa diamond anvils were used in an infrared (IR) experiment to avoid the absorption band at 1000–1300 cm^{-1}. For the IR experiments of the powder sample, T301 stainless steel gaskets were pre-indented to a thickness of 20 µm, and holes with a diameter of 160 µm were drilled at the center of the indentations to serve as the sample chamber. The sample was ground in an agate mortar and loaded into the sample chamber. For the IR experiment of the single crystal sample, rhenium (Re) gasket was pre-indented to a thickness of 50 µm, and a hole with a diameter of 200 µm was drilled to serve as the sample chamber. Naphthalene single crystal with suitable size was selected and loaded into the sample chamber. The pressure was calibrated by ruby fluorescence [38]. For all the powder experiments performed in the DAC, no pressure-transmitting medium (PTM) was employed. Ne was used as the PTM to prevent single-crystal fracture during compression in the IR experiments of the single-crystal sample.

4.2 | IR Absorption Spectra Experiments

IR experiments were performed on a Bruker VERTEX 70v with HYPERION 2000 microscope. A Globar was used as a conventional source. The spectra were collected in the transmission mode in the range of 600–4000 cm^{-1} and the resolution was 2 cm^{-1}. The absorption spectrum of the diamond anvil through the same aperture was used as the background. In the IR experiments of the single crystal sample, the single crystal was heated at 300°C for 3 h to promote the polymerization reaction after reaching the maximum pressure (30 GPa).

4.3 | X-Ray Diffraction Experiment of DAC Sample Decompressed From 30 GPa

The powder sample was loaded into a diamond anvil cell (DAC) with a T301 stainless steel sample chamber (40 μm thick), compressed to 30 GPa, and held at this pressure for 24 h. Subsequently, the pressure was decompressed to 0.7 GPa and X-ray diffraction (XRD) data was collected. The XRD data were collected at 15U1 beamline of Shanghai Synchrotron Radiation Facility (SSRF). The wavelength of the incident X-ray was 0.6199 Å. Dioptas [39] was used for data reduction.

4.4 | In Situ Neutron Diffraction

In situ neutron diffraction data were collected at BL11 PLANET, J-PARC [40] using a VX4 Paris-Edinburgh (PE) press equipped with double-toroidal sintered diamond anvils (3 mm diameter) and Titanium-Zirconium (TiZr) alloy gasket. Pressure was determined using the calibration curve of the instrument [41]. The data were collected in the range of 0–20.0 GPa, corresponding to an oil pressure range of 0–960 bar. A mixture of deuterated methanol and deuterated ethanol (4:1 v/v) was employed as the pressure-transmitting medium (PTM). Benzene-d_6 was mixed with PTM at a volume ratio of 7.5:1, and loaded into the press at low temperature. In situ neutron diffraction data at 1.3, 2.0, 3.0, 4.1, 5.0, 7.0, 9.2, 11.2, 13.1, 15.1, 17.1 and 20.0 GPa (corresponding oil pressures of 70, 110, 160, 220, 260, 360, 460, 550, 640, 730, 820 and 960 bar, respectively) were collected for 60, 60, 60, 60, 60, 60, 60, 60, 120, 120, 120 and 120 min, respectively. Naphthalene-d_8 and anthracene-d_{10} were each ground for 15 min and loaded into the sample chambers together with PTM. For naphthalene-d_8, the diffraction data at 1.3, 2.0, 3.2, 4.1, 5.2, 7.0, 9.2, 12.0, 14.0, 16.2, 18.1 and 20.0 GPa (corresponding oil pressures of 70, 110, 170, 220, 270, 360, 460, 590, 680, 780, 870 and 960 bar, respectively) were collected for 120, 40, 40, 40, 32, 55, 35, 40, 120, 120, 90, 90 min, respectively. For anthracene-d_{10}, the diffraction data at 1.3, 2.0, 3.0, 3.9, 6.0, 7.9, 9.0, 10.1, 12.9, 17.1 and 20.0 GPa (corresponding oil pressures of 70, 110, 160, 210, 310, 400, 450, 500, 630, 820 and 960 bar, respectively) were collected for 150, 120, 180, 60, 60, 60, 120, 67, 120, 120 and 212 min, respectively. The rates of the compression and decompression were kept at ~0.2 GPa/min (10 bar/min) below 10 GPa (500 bar) and ~0.1 GPa/min (5 bar/min) at 10–20 GPa (500–960 bar). Jana2006 was used for the Lebail fitting and Rietveld refinement [42].

4.5 | Synthesis of the Sample (PE20) Recovered From 20 GPa and the Sample (PE30) Recovered From 30 GPa by Paris–Edinburgh Press

The samples were synthesized using a VX3 PE press equipped with stainless steel gaskets. Double-toroidal sintered diamond anvils were used in the synthesis of the samples, and the sample volume is 10 mm^3. No PTM was used. An automatic hydraulic oil syringe pump was used to drive the PE press, and the pressure was estimated according to the Edinburgh group calibration curve [41]. The target pressure of PE20 was 20 GPa, while that of PE30 was 30 GPa, corresponding to oil pressures of 960 and 1400 bar, respectively. The samples were maintained at target pressure for about 18 h and then decompressed to ambient pressure. The rates of the compression and decompression were as follows: ~0.2 GPa/min below 4 GPa, ~0.13 GPa/min from 4 to 9 GPa, ~0.09 GPa/min from 9 to 17 GPa, ~0.04 GPa/min from 17 to 21 GPa, ~0.01 GPa/min from 21 to 30 GPa (corresponding to oil pressure: 10 bar/min below 200 bar, 6 bar/min from 200 to 400 bar, 4 bar/min from 400 to 800 bar, 2 bar/min from 800 to 1000 bar, 0.5 bar/min from 1000 to 1400 bar). After removing the unreacted naphthalene with *n*-hexane, PE30-washed and PE20-washed were obtained. PE30-washed was used in X-ray diffraction (XRD), transmission electron microscopy (TEM) and solid-state nuclear magnetic resonance (ssNMR) experiments. PE20 was dissolved in dichloromethane and used for gas chromatography-mass spectrometry (GC-MS) and direct exposure probe-mass spectrometry (DEP-MS) to analyze the oligomers.

4.6 | Characterization of PE30-Washed by X-Ray Diffraction, High-Resolution Transmission Electron Microscope (TEM), and Selected Area Electron Diffraction (SAED)

The X-ray diffraction experiment of PE30-washed was performed on a PANalytical Empyrean diffractometer (monochromatized Cu K_α radiation; $\lambda = 1.5418$ Å), and the data were recorded from 5° to 120°. The high-resolution TEM and SAED patterns were recorded on JEM-ARM200F (NEOARM) under a voltage of 80 kV.

4.7 | High-Resolution Gas Chromatography-Mass Spectrometry Measurement (GC-MS) of PE20 and the Standard Samples (1,1'-binaphthyl, 2,2'-binaphthyl, and benzo[a]anthracene), and Direct Exposure Probe-Mass Spectrometry (DEP-MS) of PE20

The PE20 was dissolved in dichloromethane (CH_2Cl_2, high-performance liquid chromatography purity, 99.9%), and the supernatant was measured by GC-MS. GC-MS measurement was performed on Thermo Scientific Q Exactive GC hybrid quadrupole-Orbitrap mass spectrometer. A TG-5SilMS capillary column (30 m × 0.25 mm inner diameter × 0.25 μm film thickness) was used, and helium (99.999%) was used as a carrier gas with a constant flow rate of 1.0 mL/min. 1 μL of the supernatant was injected manually. The temperature of GC oven was set from 40°C to 290°C at a rate of 2°C/min, and the temperature of the transfer lines was set at 260°C. The system was operated with an electron ionization source (EI) at 70 eV. The temperature of the ion source is 290°C. Scan spectra were recorded in the range of 50–750 m/z. The standard samples were characterized by GC-MS under the same experimental conditions. For DEP-MS experiment, PE-20 was also extracted by dichloromethane. High-resolution DEP-MS measurement was performed on Thermo Scientific Q Exactive GC Orbitrap MS with Direct-Exposure Probe, which features a heating filament and is capable of flash vaporization or pyrolysis up to 2000°C.

4.8 | ^{13}C Cross-Polarization Magic Angle Spinning (CP/MAS) and Quantitative Full Relaxed Direct-Polarization (DP) Solid-State Nuclear Magnetic Resonance (ssNMR) Experiments of PE30-Washed

The ^{13}C CPMAS and DP ssNMR were performed on a Bruker Avance NEO 600 MHz NMR spectrometer with a Bruker 1.3 mm double resonance MAS NMR probe. The sample was loaded into 1.3 mm ZrO_2 rotors. The MAS frequency was set to 20 kHz. The contact time is 4000 µs. About 7152 scans were accumulated for the CP spectra, and the recycle delay was 3 s. The quantitative ^{13}C NMR spectra were measured by DP with proton decoupling. About 12160 scans were accumulated for the DP spectra, and the recycle delay was 25 s. The carbon chemical shifts were referenced externally to the secondary carbon atom of adamantane at 38.48 ppm.

4.9 | Density Functional Theory Calculation

The geometry optimization of the Cambridge Sequential Total Energy Package (CASTEP) [43] module in Material Studio was used to optimize the crystal structures of naphthalene under different pressures and the product models. The optimizations were worked out with the generalized gradient approximation (GGA) in the form of Perdew–Burke-Ernzerhof (PBE) parametrization [44]. Generated on the fly (OTFG) norm-conserving pseudopotential with a 720 eV energy cutoff and a k-point resolution of $2\pi \times 0.05$ Å^{-1} was used in IR calculation at ambient pressure.

Acknowledgments

This work was supported by the National Key Research and Development Program of China (Nos. 2023YFA1406200 and 2019YFA0708502). The authors acknowledge the support of the National Natural Science Foundation of China (NSFC) (Grant No.: 22022101). The neutron experiments at the Materials and Life Science Experimental Facility of the J-PARC were performed under the user programs (Proposal Nos. 2023A0131; 2023B0030). This study was partially supported by 4W2 beamline at Beijing Synchrotron Radiation Facility (BSRF), 15U1 beamline at Shanghai Synchrotron Radiation Facility (SSRF) and BL10XU of Spring-8. The authors also acknowledge Synergic Extreme Condition User Facility (SECUF).

Conflicts of Interest

The authors declare no conflicts of interest.

Data Availability Statement

The data that support the findings of this study are available in the supplementary material of this article.

References

1. X. Wen, R. Hoffmann, and N. W. Ashcroft, "Benzene Under High Pressure: A Story of Molecular Crystals Transforming to Saturated Networks, With a Possible Intermediate Metallic Phase," *Journal of the American Chemical Society* 133 (2011): 9023–9035.

2. D. Stojkovic, P. Zhang, and V. H. Crespi, "Smallest Nanotube: Breaking the Symmetry of sp^3 Bonds in Tubular Geometries," *Physical Review Letters* 87 (2001): 125502.

3. J. F. R. V. Silveira and A. R. Muniz, "First-Principles Calculation of the Mechanical Properties of Diamond Nanothreads," *Carbon* 113 (2017): 260–265.

4. R. E. Roman, K. Kwan, and S. W. Cranford, "Mechanical Properties and Defect Sensitivity of Diamond Nanothreads," *Nano Letters* 15 (2015): 1585–1590.

5. H. Zhan, G. Zhang, V. B. C. Tan, et al., "From Brittle to Ductile: A Structure Dependent Ductility of Diamond Nanothread," *Nanoscale* 8 (2016): 11177–11184.

6. H. Zhan, G. Zhang, J. M. Bell, and Y. Gu, "The Morphology and Temperature Dependent Tensile Properties of Diamond Nanothreads," *Carbon* 107 (2016): 304–309.

7. J. Xue, Y. Xie, Q. Peng, and Y. Chen, "Thermal Transports of One-Dimensional Ultrathin Carbon Structures," *Nanotechnology* 30 (2019): 475401.

8. H. Zhan, G. Zhang, Y. Zhang, V. B. C. Tan, J. M. Bell, and Y. Gu, "Thermal Conductivity of a New Carbon Nanotube Analog: The Diamond Nanothread," *Carbon* 98 (2016): 232–237.

9. T. C. Fitzgibbons, M. Guthrie, E.-S. Xu, et al., "Benzene-Derived Carbon Nanothreads," *Nature Materials* 14 (2015): 43–47.

10. X. Li, M. Baldini, T. Wang, et al., "Mechanochemical Synthesis of Carbon Nanothread Single Crystals," *Journal of the American Chemical Society* 139 (2017): 16343–16349.

11. B. Maryasin, M. Olbrich, D. Trauner, and C. Ochsenfeld, "Calculated Nuclear Magnetic Resonance Spectra of Polytwistane and Related Hydrocarbon Nanorods," *Journal of Chemical Theory and Computation* 11 (2015): 1020–1026.

12. P. Duan, X. Li, T. Wang, et al., "The Chemical Structure of Carbon Nanothreads Analyzed by Advanced Solid-State NMR," *Journal of the American Chemical Society* 140 (2018): 7658–7666.

13. T. Wang, P. Duan, E.-S. Xu, et al., "Constraining Carbon Nanothread Structures by Experimental and Calculated Nuclear Magnetic Resonance Spectra," *Nano Letters* 18 (2018): 4934–4942.

14. X. Yang, G. Che, Y. Wang, et al., "High-Pressure Polymerization of Phenol Toward Degree-4 Carbon Nanothread," *Nano Letters* 25 (2025): 1028–1035.

15. G. Che, X. Tang, J. Liu, et al., "Pressure-Driven Solid-State Radical Polymerization Toward Carbon Nanothread," *Nano Letters* 25 (2025): 14467–14472.

16. G. Che, X. Tang, P. Lang, et al., "Fluorine-Directed Structure-Specific Carbon Nanothreads," *Chemistry: A European Journal* 31 (2025): e202501735.

17. X. Li, T. Wang, P. Duan, et al., "Carbon Nitride Nanothread Crystals Derived From Pyridine," *Journal of the American Chemical Society* 140 (2018): 4969–4972.

18. S. G. Dunning, L. Zhu, B. Chen, et al., "Solid-State Pathway Control via Reaction-Directing Heteroatoms: Ordered Pyridazine Nanothreads Through Selective Cycloaddition," *Journal of the American Chemical Society* 144 (2022): 2073–2078.

19. A. Biswas, M. D. Ward, T. Wang, et al., “Evidence for Orientational Order in Nanothreads Derived From Thiophene,” *Journal of Physical Chemistry Letters* 10 (2019): 7164–7171.

20. X. Wang, X. Yang, Y. Wang, et al., “From Biomass to Functional Crystalline Diamond Nanothread: Pressure-Induced Polymerization of 2,5-Furandicarboxylic Acid,” *Journal of the American Chemical Society* 144 (2022): 21837–21842.

21. P. G. Demingos and A. R. Muniz, “Carbon Nanothreads From Polycyclic Aromatic Hydrocarbon Molecules,” *Carbon* 140 (2018): 644–652.

22. X. Yang, G. Che, F. Li, et al., “Fused-ring Carbon Nanothread Synthesized by Pressure-induced Polymerization of Azulene,” *Journal of Physical Chemistry C* 128 (2024): 16011–16019.

23. M. D. Ward, W. S. Tang, L. Zhu, D. Popov, G. D. Cody, and T. A. Strobel, “Controlled Single-crystalline Polymerization of $C_{10}H_8{\cdot}C_{10}F_8$ Under Pressure,” *Macromolecules* 52 (2019): 7557–7563.

24. A. Friedrich, I. E. Collings, K. F. Dziubek, et al., “Pressure-Induced Polymerization of Polycyclic Arene-Perfluoroarene Cocrystals: Single Crystal X-Ray Diffraction Studies, Reaction Kinetics, and Design of Columnar Hydrofluorocarbons,” *Journal of the American Chemical Society* 142 (2020): 18907–18923.

25. Z. Zhao, G. Che, F. Li, et al., “Synthesis of a Biphenylene Nanoribbon by Compressing Biphenylene Under Extreme Conditions,” *Physical Chemistry Chemical Physics* 27 (2025): 6072–6078.

26. G. Che, Y. Fei, X. Tang, et al., “Pressure-induced Polymerization of 1,4-Difluorobenzene Towards Fluorinated Diamond Nanothreads,” *Physical Chemistry Chemical Physics* 27 (2025): 1112–1118.

27. B. Chen, R. Hoffmann, N. W. Ashcroft, J. Badding, E. Xu, and V. Crespi, “Linearly Polymerized Benzene Arrays as Intermediates, Tracing Pathways to Carbon Nanothreads,” *Journal of the American Chemical Society* 137 (2015): 14373–14386.

28. A. Guijarro, J. A. Vergés, E. San-Fabián, G. Chiappe, and E. Louis, “Herringbone Pattern and CH–π Bonding in the Crystal Architecture of Linear Polycyclic Aromatic Hydrocarbons,” *Chemie Physikalische Chemie* 17 (2016): 3548–3557.

29. E. O’ Bannon and Q. Williams, “Vibrational Spectra of Four Polycyclic Aromatic Hydrocarbons Under High Pressure: Implications for Stabilities of PAHs During Accretion,” *Physics and Chemistry of Minerals* 43 (2016): 181–208.

30. K. P. Meletov, “Phonon Spectrum of a Naphthalene Crystal at a High Pressure: Influence of Shortened Distances on the Lattice and Intramolecular Vibrations,” *Physics of the Solid State* 55 (2013): 581–588.

31. A. Y. Likhacheva, S. V. Rashchenko, A. D. Chanyshev, T. M. Inerbaev, K. D. Litasov, and D. S. Kilin, “Thermal Equation of state of Solid Naphthalene to 13 GPa and 773 K: In Situ X-Ray Diffraction Study and First Principles Calculations,” *Journal of Chemical Physics* 140 (2014): 164508.

32. A. Y. Likhacheva, S. V. Rashchenko, and K. D. Litasov, “High-Pressure Structural Properties of Naphthalene up to 6 GPa,” *Journal of Applied Crystallography* 47 (2014): 984–991.

33. A. Shinozaki, K. Mimura, T. Nishida, T. Inoue, S. Nakano, and H. Kagi, “Stability and Partial Oligomerization of Naphthalene Under High Pressure at Room Temperature,” *Chemical Physics Letters* 662 (2016): 263–267.

34. M. Murphy, S. Huss, B. Xu, et al., “High-Pressure Synthesis of Carbon Nanothreads From Polycyclic Aromatic Hydrocarbons,” *ACS Materials Au* (2025), https://doi.org/10.1021/acsmaterialsau.5c00178.

35. L. Ciabini, M. Santoro, R. Bini, and V. Schettino, “High Pressure Reactivity of Solid Benzene Probed by Infrared Spectroscopy,” *Journal of Chemical Physics* 116 (2002): 2928–2935.

36. A. Shinozaki, K. Mimura, H. Kagi, K. Komatu, N. Noguchi, and H. Gotou, “Pressure-Induced Oligomerization of Benzene at Room Temperature as a Precursory Reaction of Amorphization,” *Journal of Chemical Physics* 141 (2014): 084306.

37. L. Ciabini, M. Santoro, F. A. Gorelli, R. Bini, V. Schettino, and S. Raugei, “Triggering Dynamics of the High-pressure Benzene Amorphization,” *Nature Materials* 6 (2007): 39–43.

38. H. K. Mao, J. Xu, and P. M. Bell, “Calibration of the Ruby Pressure Gauge to 800 Kbar Under Quasi-Hydrostatic Conditions,” *Journal of Geophysical Research* 91 (1986): 4673–4676.

39. C. Prescher and V. B. Prakapenka, “Dioptas: A Program for Reduction of Two-Dimensional X-Ray Diffraction Data and Data Exploration,” *High Pressure Research* 35 (2015): 223–230.

40. T. Hattori, A. Sano-Furukawa, H. Arima, et al., “Design and Performance of High-Pressure PLANET Beamline at Pulsed Neutron Source at J-PARC,” *Nuclear Instruments and Methods in Physics Research* 780 (2015): 55–67.

41. T. Hattori, A. Sano-Furukawa, S. Machida, et al., “Development of a Technique for High Pressure Neutron Diffraction at 40 GPa with a Parisedinburgh Press,” *High Pressure Research* 39 (2019): 417–425.

42. V. Petříček, M. Dušek, and L. Palatinus, “Crystallographic Computing System JANA2006: General Features,” *Zeitschrift für Kristallographie – Crystalline Materials* 229 (2014): 345–352.

43. S. J. Clark, M. D. Segall, C. J. Pickard, et al., “First Principles Methods Using CASTEP,” *Zeitschrift für Kristallographie – Crystalline Materials* 220 (2005): 567–570.

44. J. P. Perdew, K. Burke, and M. Ernzerhof, “Generalized Gradient Approximation Made Simple,” *Physical Review Letter* 77 (1996): 3865–3868.

Supporting Information

Additional supporting information can be found online in the Supporting Information section.

Supporting File: Additional supporting information can be found in the Supporting Information section.